Synthesis and characterisation of the vibrational and electrical properties of antiferromagnetic 6L-Ba2CoTeO6 ceramics

AZIZ, A.A., MERCONE, S., LOBO, R.P.S.M., DIAS, A., MOREIRA, R.L., BELL, Anthony <http://orcid.org/0000-0001-5038-5621>, ECCLESTON, R. and FETEIRA, A.

Dalton Transactions

PAPER

Cite this: DOI: 10.1039/c9dt00418a

Synthesis and characterisation of the vibrational and electrical properties of antiferromagnetic 6L-Ba_2CoTeO_6 ceramics†

Anees A. Aziz, [a,b] Silvana Mercone, [c] Ricardo P. S. M. Lobo, [d,e] Anderson Dias, [f] Roberto L. Moreira, [g] Anthony M. T. Bell, [a] Roger Eccleston[a] and Antonio Feteira *[a]

Received 29th January 2019,
Accepted 16th June 2019

DOI: 10.1039/c9dt00418a

rsc.li/dalton

Optimal processing conditions for fabrication of dense single-phase 6L-Ba_2CoTeO_6 ceramics *via* the solid-state reaction method were determined. These ceramics possess a room-temperature crystal structure described by the centrosymmetric $P\bar{3}m1$ space group. Polarized Raman spectroscopy enabled the observation of all the 25 predicted Raman modes and assignment of their symmetries. On cooling, BCTO ceramics exhibit two antiferromagnetic transitions at 3 K and 12.5 K, in broad agreement with a recent single-crystal study [P. Chanlert, N. Kurita, H. Tanaka, D. Goto, A. Matsuo and K. Kindo, Phys. Rev. B: Condens. Matter Mater. Phys., 2016, 93, 094420]. Low temperature Fourier-transform infrared reflectivity analyses suggest the antiferromagnetic phase transitions to be driven by small distortions of the CoO_6 octahedra, lowering locally their C_{3v} symmetry. This causes splitting of the associated vibrational modes, but without a long-range structural change. AC impedance spectroscopy revealed BCTO ceramics to be leaky insulators with an activation energy for conduction of ~0.15–0.25 eV, which suggests electron hopping between mixed oxidation states of Co.

1. Introduction

Perovskite (ABO_3)-based ceramics are widely employed in the fabrication of electrical and electronic components such as capacitors,[1] PTCRs,[2] microwave resonators[3] and piezoelectrics.[4,5] Invariably, those components are based on perovskites whose crystal structures follow an *abc* cubic closed-packed stacking sequence of AO_3 layers with B cations occupying octahedral interstices. This sequence is commonly referred to as a 3C-structure and is characterised by corner-sharing BO_6 octahedra. Nevertheless, in the case where AO_3 layers adopt a hexagonal close-packing stacking sequence *ab*, then face-sharing octahedra are formed, which is the typical motive of hexagonal perovskites.[6–9] Moreover, between these two ideal packing sequences, the possibility exists for the occurrence of intermediate structures containing different proportions of corner- and face-sharing octahedra forming chains along the hexagonal *c*-axis. Hexagonal perovskite variants have been known since the early 1960s.

Nowadays, it is generally accepted that they are less common than their cubic counterparts, because typically they only crystallise when A cations are too large to be accommodated within a framework of corner-sharing BO_6 octahedra.

Historically, Ba_2CoTeO_6 (BCTO) is amongst the first hexagonal perovskites to have been synthesised, however initially this compound was erroneously reported as a cubic perovskite. In 1963, Gerhard Bayer[10] prepared several Te-compounds with the general formula A_2MgTeO_6, where A = Ba, Sr, Pb, (Pb,Sr) and (Pb,Ba), encompassing 6-fold coordinated Te^{6+}. These compounds were reported to crystallise in the cubic $Fm\bar{3}m$ space group. Details on the synthesis procedures of a wider variety of $A_2^{2+}BTeO_6$ compositions (where A = Ca, Sr, Ba, Pb and B = Ca, Cd, Zn, Co, Cu, Ni and Mg) were later presented in a patent,[11] claiming the compounds to be ferroelectric, but without any experimental evidence. BCTO was reported to crystallised in a cubic structure with a lattice constant, a = 8.37 Å. In 1972, Köhl *et al.*[12] studied Ba_2NiTeO_6 (BNTO) in detail and

[a]Christian Doppler Lab in Advanced Ferroic Oxides, Materials and Engineering Research Institute, Sheffield Hallam University, Howard Street, Sheffield, UK. E-mail:. E-mail: a.feteira@shu.ac.uk
[b]Faculty of Electrical Engineering, Universiti Teknologi MARA, 40450 Shah Alam, Selangor, Malaysia
[c]LSPM, CNRS UPR 3407, Université Paris Nord, Sorbonne Paris Cité, 99 Avenue J.-B. Clément, 93430 Villetaneuse, France
[d]LPEM, ESPCI Paris, PSL University, CNRS, F-75005 Paris, France
[e]Sorbonne Université, CNRS, LPEM, F-75005 Paris, France
[f]Departamento de Química, ICEx, Universidade Federal de Minas Gerais, 30123-970 Belo Horizonte, Minas Gerais, Brazil
[g]Departamento de Física, ICEx, Universidade Federal de Minas Gerais, C.P. 702, 30123-970 Belo Horizonte, Minas Gerais, Brazil

†Electronic supplementary information (ESI) available: SEM of powder, processing conditions and densities, CIE LAB coordinates, EDAX, Rietveld refinement, AC impedance. See DOI: 10.1039/c9dt00418a

proposed this compound to crystallised as a 12-layer hexagonal perovskite, with a = 5.797 Å and c = 28.595 Å. This structure was described as consisting of a framework of three face-sharing octahedra connected by one corner-sharing octahedron. Ba_2BTeO_6 (where B = Ni, Zn or Co) were also suggested to be hexagonal perovskites, whereas Ba_2MgTeO_6 was reported to be a cubic perovskite. Liegeois-Duyckaerts[13] compared the infrared and Raman spectra of Ba_2BTeO_6 (where B = Ni, Zn or Co) and found the Co-based compound to exhibit an infrared spectrum significantly different from that of the Zn- and Ni-compounds; the latter spectra were nearly indistinguishable. In 1985, Liegeois-Duyckaerts[14] reported BCTO to be a 6-layer hexagonal perovskite, with a = 5.80 Å and c = 14.23 Å, crystallising in the $P\bar{3}m1$ space group. In this instance, the structure consists of two face-sharing octahedra connected by one corner-sharing octahedron, similar to that of hexagonal $BaTiO_3$. Some ordering between the B-site cations was proposed. This structural determination was further corroborated by neutron diffraction analysis carried out by Ivanov *et al.*,[15] who also showed the absence of any structural transitions between 5 and 295 K. Ba_2CrMoO_6,[16] Ba_2CoOsO_6, and Ba_2NiOsO_6 [17] are other compounds that were also reported to adopt the 6-layered $BaTiO_3$-type structure.

Several scientists[18–20] investigated the possibility of developing high Curie temperature ferroelectric perovskites based on Te^{6+}, because of its high charge and small ionic radii (0.56 Å), which could favour the formation of an electric dipole. Although BCTO was claimed to be antiferroelectric, the necessary evidence in the form of a polarisation *vs.* electric field (*P–E*) double loop[19] data was not provided. In 2010, Ivanov *et al.*[15] also commented on the absence of a *P–E* hysteresis loop up to the breakdown field of BCTO ceramics.

In principle, the occurrence of ferroelectricity in BCTO can be ruled out. First, from a structural viewpoint, BCTO cannot be ferroelectric because its internal average crystal symmetry is described by a centrosymmetric space group, thereby precluding the presence of any spontaneous polarisation. Second, according to modern ferroelectric theories, d^0-orbitals are an essential requirement for B-site driven ferroelectricity in perovskites.[21,22] This requirement is not met in BCTO, because Te^{6+} and Co^{2+} have $4d^{10}$ and $3d^7$ electronic configurations, respectively.

Finally, the magnetic behaviour of BCTO arises exclusively from Co^{2+} ions. Ivanov *et al.*[15] reported antiferromagnetic (AFM) ordering below $T_N \approx 15$ K, with spins roughly parallel to the c axis with a canting angle of 24.5°.[15,23] More recently, an investigation using BCTO single-crystals revealed two successive AFM phase transitions, at 12.0 K and 3.0 K, arising from independent spin ordering of two decoupled subsystems associated with the two inequivalent Co^{2+} ions.[24] Indeed, BCTO belongs to a hexagonal $P\bar{3}m1$ space group,[15] where two inequivalent divalent Co ions form two sub-lattices, one composed of almost cubic $Co(1)O_6$ octahedra and another of non-centrosymmetric $Co(2)O_6$ octahedra. Because of such a difference, each subsystem orders at a different temperature, *via* a different and particular mechanism: subsystem A, formed by $Co(1)O_6$ ordering at 3.0 K, subsystem B, formed by $Co(2)O_6$ ordering at 12.0 K.[24] As a result, the magnetic susceptibility is anisotropic showing a strong dependence on the crystal direction along which the magnetic field is applied and presents a maximum at around 20 K, with an inflection point at 15.0 K and a bend anomaly at 3.0 K. This low temperature AFM transition was observed to shift to lower temperature when the field was applied parallel to the c-axis of the single-crystal. Recent work[25] conducted at Los Alamos National Laboratory involving magnetostriction experiments in pulsed magnetic fields up to 60 Tesla provided data to construct a H–T phase diagram for H parallel and perpendicular to the c-axis of BCTO crystals. These preliminary data suggest a strong magnetocaloric effect.

Our work presents, for the first time, a comprehensive investigation of the processability of single-phase BCTO ceramics. To verify the existence of the magnetic transitions in BCTO ceramics, magnetization curves were recorded at different magnetic fields using zero-field-cooled (ZFC) and field-cooled (FC) procedures. Optical-vibrational spectroscopic techniques were employed to investigate the phonon modes behavior and to appraise the origin of the low temperature magnetic transitions. Finally, the bulk electrical conductivity was extracted from AC impedance analysis.

2. Experimental

Dried $BaCO_3$ (>99.9%, Sigma-Aldrich), TeO_2 (≥99%, Sigma-Aldrich) and Co_3O_4 (>99.9%, Sigma-Aldrich) powders were weighed according to the Ba_2CoTeO_6 formula. These powders were placed into a 250 ml milling polyethylene bottle together with yttrium-stabilized zirconia milling media and propan-2-ol and then mixed on a roller ball mill overnight. Mixed powders were dried and then passed through a 500 μm mesh sieve. The sieved powders were reacted according to the firing schedules given in Table S1 in the ESI.† Intermittent re-grinding and re-firing was carried out until no change on X-ray diffraction (XRD) data was perceptible. The fully reacted powders were then pressed as 10 mm pellets and fired up to 1425 °C for 4 hours. The pellets were covered with BCTO loose powder and sintered in a closed alumina crucible to limit loss of Te and Co. Purity and crystal structure analyses were carried out by X-ray powder diffraction (XRD) using a PANalytical diffractometer (Empyrean) set up in reflection geometry and using monochromatic Cu $K\alpha_1$ radiation. XRD patterns were acquired in the 10–65 2θ range, with a step size of 0.0131 2θ degrees with a scan length of 2 seconds per step. For powder prepared at 1000 °C, XRD experiments were carried out using Co $K\alpha_1$ radiation and Rietveld Refinement of the data is given in Fig. S1 and Table S2 in the ESI.† Ceramic microstructures were characterised using a FEI scanning electron microscope (Nova) equipped with a field emission gun. Microchemical analysis was carried out using an EDAX system and results are provided in the ESI.†

The magnetic susceptibility of the Ba_2CoTeO_6 ceramic was obtained in the temperature range of 2–50 K using a Quantum

Design SQUID-VSM magnetometer. The DC magnetization measurements were recorded in two different magnetic fields (0.5 Tesla and 1 Tesla), performing a zero-field-cooled (ZFC) and field-cooled (FC) procedures. The temperature dependencies of raw magnetic susceptibilities ($\chi = M/H$) can be thus calculated. We show here the magnetic susceptibilities behaviour well below the nitrogen temperature ($T < 50$ K) where the effective spin-1/2 description of the Co^{2+} spin in an octahedral environment is valid.[26]

Un-polarized and polarized Micro-Raman scattering spectra of BCTO ceramic samples were recorded at room temperature using a Horiba/Jobin–Yvon LABRAM-HR spectrometer, equipped with a LN_2-cooled CCD detector and a confocal Olympus microscope (100× objective). The spectral resolution was *circa* 1 cm^{-1} (diffraction grating of 1800 grooves per mm) and the spatial resolution around 1 μm. The measurements were carried out in back-scattering geometry, using the 633 nm line of He–Ne laser (6 mW at the sample's surface) as the excitation source. Appropriate interference and edge filters, half-wave plate and polarizers were used. The spectra were obtained between 40 and 900 cm^{-1}, by averaging 10 accumulations of 30 s, and corrected for the Bose–Einstein thermal factor.[27] Fourier transform infrared (FTIR) reflection spectra of BCTO were collected with a Bruker IFS66v, from room-temperature down to 5 K. Appropriate sources, beamsplitters (BMS) and detectors were used for different spectral regions, namely Hg-arc lamp, Ge coated mylar BMS and 4 K Si:B-bolometer for the far-infrared region (30–700 cm^{-1}); SiC globar source, KBr:Ge BMS, 4 K Si:B photoconductor, for the mid-infrared region (500–2500 cm^{-1}). Reference spectra were taken by *in situ* evaporation of gold onto the sample surface, after a complete temperature cycle of measurements on the sample. Reference spectra were also taken for each measured temperature, in order to correct for instrumental drifts. By using this procedure, mid and far infrared spectra matched well in the superposition region (within 1–2%). All measurements were performed under vacuum, with 2 cm^{-1} of spectral resolution, by averaging at least 128 scans. AC impedance spectroscopy was carried out between 298 to 673 K using an Agilent E4980A. For these measurements, silver electrodes were applied to both faces of the ceramic disks prepared at 1350 °C.

3. Results and discussion

3.1 Synthesis of Ba_2CoTeO_6 powders

Room-temperature XRD patterns for mixed raw materials reacted at 500, 700, 900, 1000 and 1100 °C are illustrated in Fig. 1. After reaction at 500 °C for 12 h, the powder consists mainly of unreacted $BaCO_3$, Co_3O_4 (as indicated by the dotted ellipsoids), TeO_2 and some $BaTe_2O_5$, as an intermediate phase. In the past, Kwon *et al.*[28] observed the formation of $BaTe_2O_5$ in a $2BaCO_3 : 1TeO_2$ mixture to occur at ~550 °C. At this stage, it is worth to mention the Te^{4+} oxidation state in both TeO_2 and $BaTe_2O_5$ phases. XRD data collected from powder prepared at

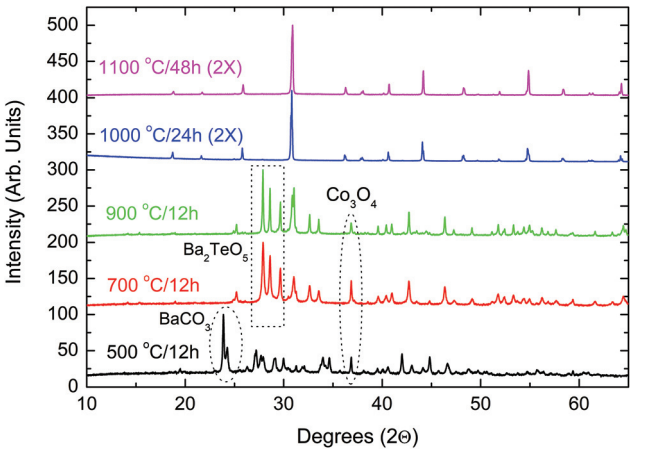

Fig. 1 Room-temperature XRD data showing phase formation of BCTO powders.

700 °C for 12 h reveals some residual Co_3O_4 but a complete consumption of $BaCO_3$ and TeO_2. That is accompanied by formation of Ba_2TeO_5 (as indicated by the dotted rectangle), which contains Te^{6+}. The oxidation of tellurium at this temperature is in broad agreement with Bayer's classical work,[10] where an almost complete oxidation of $Te^{IV}O_2$ to $Te^{VI}O_3$ was reported to occur after a heat treatment at 700 °C for 6 h. Between 700 and 900 °C, the nature of the phases present remains relatively unaltered, and the grey (Table S1 of ESI†) appearance of the powder reacted at ≤900 °C is partially imparted by the presence of Co_3O_4, a black solid of mixed valence (*i.e.* $Co^{II}Co^{III}_2O_4$). As expected, above 900 °C, Co_3O_4 decomposes according to $2Co_3O_4 \rightleftharpoons 6CoO + O_2$. This reaction results in the complete conversion of Co^{3+} (d^6) to Co^{2+} (d^7). Hence, at 1000 °C the reaction proceeds between all these intermediate phases prompting the formation of single phase 6L-Ba_2CoTeO_6, as shown by the respective XRD data, in Fig. 1.

It is worth mentioning that the colour of the reaction product changes from grey to violet, as shown in Table S1 in the ESI,† which also corroborates the change of the oxidation state of cobalt to +2. This reaction proceeds to completion as the powder appears to be single-phase, within the resolution of the technique. Indeed, all reflections can be indexed according to hexagonal perovskite 6L-Ba_2CoTeO_6. Lattice parameters were refined as $a = 5.79870(3)$ Å and $c = 14.26599(9)$ Å, showing good agreement with the previous work by Ivanov *et al.*[15] Refined structural parameters for BCTO prepared at 1000 °C are given in Table S2 of the ESI.† No difference in the XRD pattern was observed for powder fired at 1100 °C for 96 h, as shown in Fig. 1. The complete formation of BCTO in the temperature range 1000–1100 °C is comparable with the temperatures reported by Bayer[10] to synthesise Ba_2MgTeO_6 by solid-state reaction.

3.2 Fabrication of Ba_2CoTeO_6 ceramics

After milling, the reacted BCTO powder consisted mainly of flake-like particles, with sizes ranging from 1 to 10 μm, as illus-

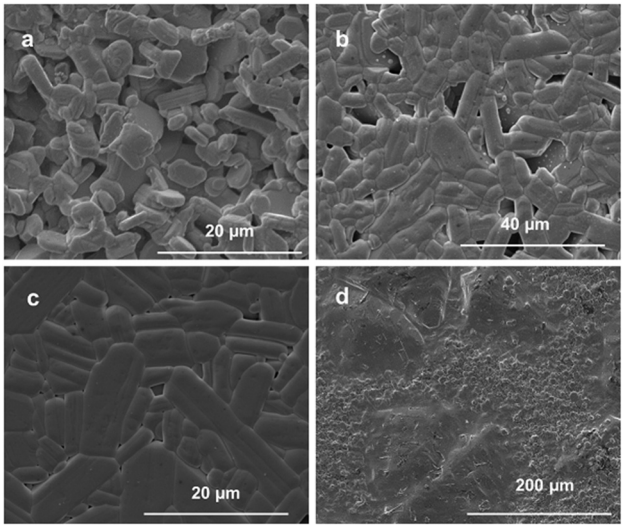

Fig. 2 Microstructural evolution of BCTO ceramics with firing temperature, for (a) 1300 °C (polished and thermally etched at 1150 °C for 1 h); (b) 1350 °C (polished and thermally etched at 1200 °C for 1 h); (c) 1400 °C (polished and thermally etched at 1250 °C for 1 h) and (d) 1425 °C (as-fired).

trated in Fig. S2 in the ESI.† Those powders were uniaxially pressed at 200 MPa to form green compacts with a relative density of ~55%. Subsequently, they were fired at temperatures ranging from 1300 °C to 1425 °C. Initially, relative densities increased with increasing firing temperatures, as shown in Table S3 in the ESI,† reaching a maximum of ~90% of the theoretical density for ceramics fired at 1400 °C. Above this temperature their relative densities slightly decreased and eventually melted at 1450 °C. The increase in the relative density was accompanied by dramatic microstructural changes as illustrated in Fig. 2(a–d). The relatively low density measured for ceramics fired at 1300 °C, is corroborated by the microstructure shown in Fig. 2a. Indeed, these ceramics consist mainly of anisometric plate-like grains exhibiting extensive necking and a three-dimensional network of open porosity.

In comparison with the initial particle size distribution (Fig. S2 in ESI†) grain growth was negligible. With increasing firing temperature, necking is replaced by well-defined grain boundaries and a concomitant reduction of porosity, as illustrated in Fig. 2b and c, for ceramics fired at 1350 °C and 1400 °C, respectively. Grain growth is accompanied by the establishment of a microstructure consisting of grains with an anisometric ratio varying between 2 and 4. Finally, ceramics fired at 1425 °C, which XRD data shown to be no longer single-phase, exhibit a bimodal microstructure consisting of large polygonal grains (>150 μm) embedded in a finer grained matrix. Room-temperature XRD patterns from the surface of ceramics sintered at 1300, 1350, 1400 and 1425 °C are illustrated in Fig. 3. These data show the appearance of a Ba_3TeO_6-based secondary phase (as indicated by the dotted ellipsoids) when the sintering temperature reaches 1400 °C, resulting from Co-loss as indicated by EDAX analysis, presented in

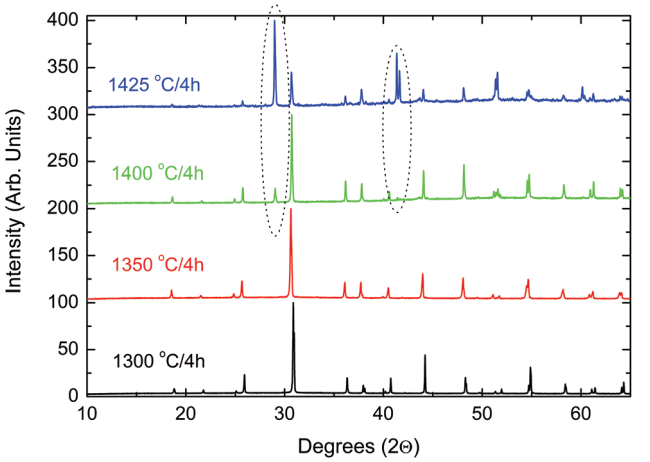

Fig. 3 Room-temperature XRD data for the as-fired surface of BCTO ceramics in function of the firing temperature.

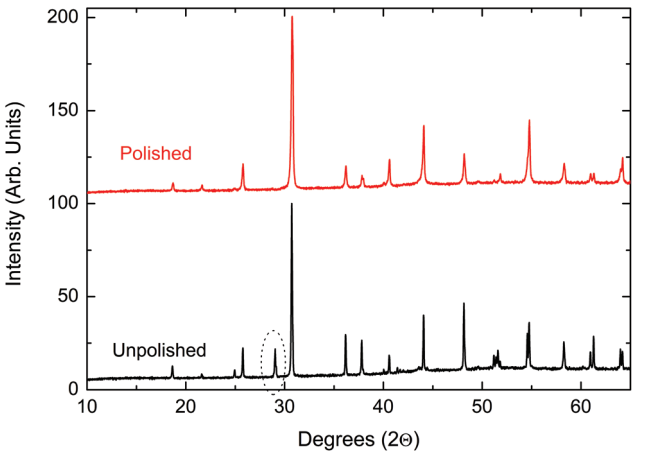

Fig. 4 Room-temperature XRD for bulk (polished) and surface (unpolished) BCTO ceramics fired at 1400 °C.

Fig. S3 of the ESI.† Eventually, at 1425 °C Ba_3TeO_6 becomes the primary phase.

The XRD data in Fig. 4, compares surface and bulk phase purity of ceramics fired at 1400 °C. Basically, XRD data was first collected from the as-fired surface and subsequently from the bulk after removing a depth of ~100 μm. It becomes evident that the bulk consists uniquely of Ba_2CoTeO_6, suggesting that decomposition occurs near the surface because of the lower Co cobalt pressure in the firing atmosphere. Hereafter the measurements of the physical properties was carried out on the single-phase ceramics prepared at 1350 °C.

3.3 Magnetic characterization of Ba_2CoTeO_6 ceramics

In order to verify the existence of magnetic transitions in BCTO ceramics, magnetization curves were recorded at different magnetic fields using ZFC and FC procedures. No visible hysteretic behavior was observed for the ZFC and FC

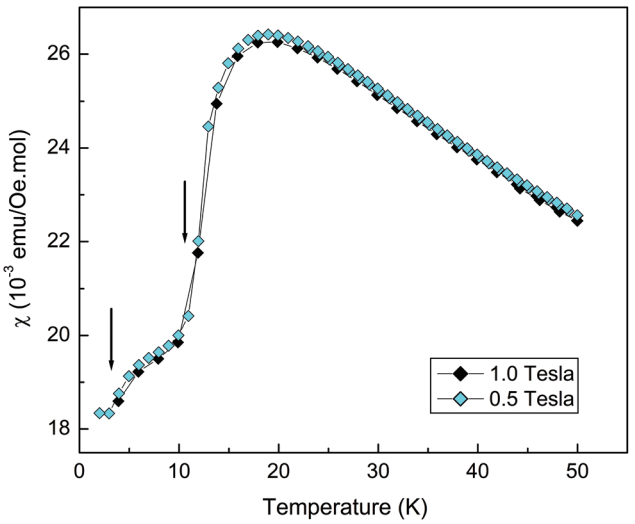

Fig. 5 Magnetic susceptibilities ($\chi = M/H$) for BCTO obtained on heating at the indicated magnetic fields. The vertical arrows indicate the two AFM phase transitions.

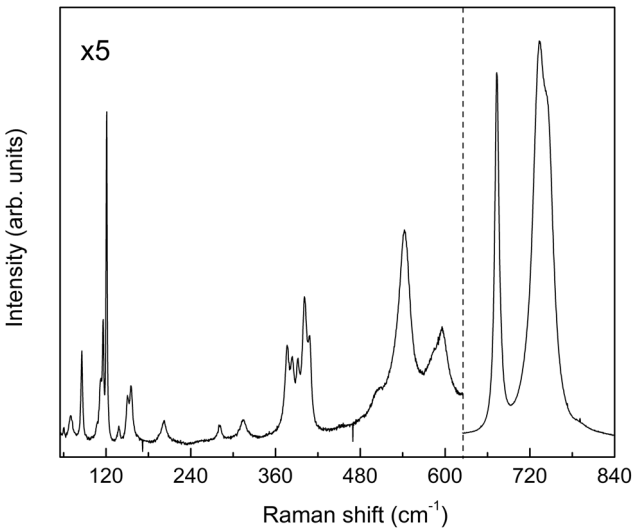

Fig. 6 Unpolarized Raman spectrum of hexagonal BCTO ceramics in the spectral region 50–840 cm^{-1}.

curves, which corroborates the order strength of the observed magnetic transitions. Hence, Fig. 5 shows the calculated susceptibilities recorded on heating between 2 K and 50 K at 0.5 T and 1.0 T, after the ZFC procedure. In Fig. 5, the arrows indicate the temperatures of the two anomalies associated to the successive AFM phase transitions. The transition temperatures were determined from the maximum of the $d(M/H \times T)/dT$ derivative. Those transitions were found at 3 K and 12.5 K, in perfect agreement with the single-crystal results.[24] Moreover, the susceptibility values found for our ceramic correspond very well to the average values of the anisotropic ones found for single-crystals,[24] *i.e.*, $\chi_{cer} = 1/3\ \mathrm{Tr}(\chi)$. In addition, the calculated Curie Weiss constant of (−145 ± 5 K) and a frustration parameter $f = -\frac{\vartheta_{CW}}{T_s} = 12$ is in good agreement with previous observations,[23] suggesting a high-spin $3d^7$ configuration of Co-cations in the ceramic sample. As reported before, this should be linked to a weaker Co–O covalency, possibly related to a simultaneous increase in the A–O one. The excellent agreement between the results of the magnetic characterization of the present ceramics and that of single-crystals corroborates the very good quality of the fabricated ceramics. It is also worth mentioning the absence of any anomaly around 40 K, which has been long established to be the Néel temperature of Co_3O_4. This reassures the complete reaction of Co_3O_4, as mentioned in section 3.1.

3.4 Polarization-resolved Raman spectra of Ba_2CoTeO_6 ceramics

Optical vibrational spectroscopies are useful techniques to correlate structure–optical behavior of crystalline insulator materials, as well as to infer about their dielectric, electric and other related properties.[29–34] These techniques allow one to obtain the optical vibrational modes at the Brillouin zone center of crystalline materials. Using several methods and group theory tools, these modes can be anticipated from knowledge of both crystal structure and occupied sites in the primitive cell. In the present case, BCTO adopts a hexagonal structure belonging to the $P\bar{3}m1$ space group, which allows the accommodation of the large Ba^{2+} cation.[15] Using the (occupied) Wyckoff sites of BCTO,[15] and applying the nuclear site method of Rousseau *et al.*,[35] shown in Table S4 in the ESI,† it was determined that BCTO should present 25 Raman-active first-order modes (11 $A_g \oplus$ 14 E_g) and 27 infrared ones (12 $A_u \oplus$ 15 E_u). Raman spectra of BCTO were obtained with unpolarized and polarized lights. Fig. 6 presents the unpolarized Raman spectrum of BCTO. In this spectrum, it is possible to discern 23 of the 25 predicted modes, because accidental degeneracy of modes of different symmetries forbids the resolution of peaks that are too close. Therefore, polarized spectra were used to resolve such modes. Despite the polycrystalline nature of the ceramic sample, it is possible to resolve their A_g and E_g modes by polarized light because the grain size (as shown in Fig. 2) is larger than the observation region (~1 μm). Thus, parallel-polarized light would favor A_g type modes (whose base functions into the D_3 point symmetry are $xx + yy$, and zz), while crossed polarized light would enhance the E_g modes ($xx - yy$, xy, xz and yz base functions).

The polarized Raman spectra of BCTO are presented in Fig. 7. Note that all the 25 predicted Raman modes could be observed by this method, and their symmetries assigned. The complete assignment of all first-order Raman modes of BCTO into its hexagonal symmetry is then presented in Table 1.

3.5 The complete set of infrared phonon modes of Ba_2CoTeO_6

The crystal symmetry of BCTO is described by the $P\bar{3}m1$ centrosymmetric space group, thereby Raman and Infrared modes belong to mutually exclusive irreducible representations. The centrosymmetric nature of BCTO was previously validated by

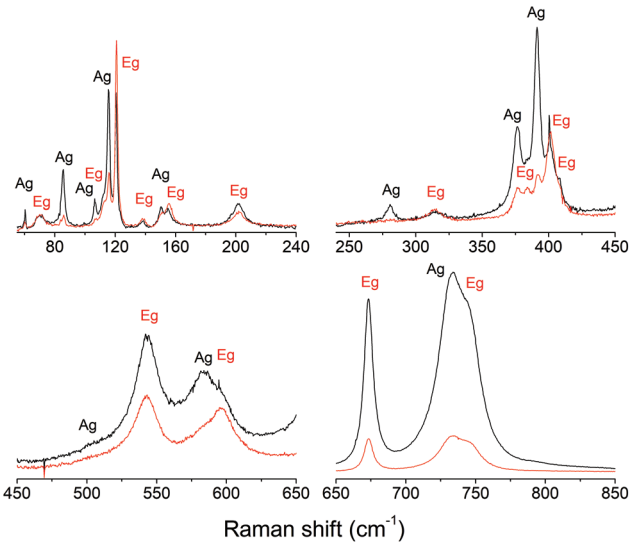

Fig. 7 Polarization-resolved Raman spectra of BCTO ceramics; black and red lines represent the parallel polarized and the crossed-polarized spectra, respectively, revealing hexagonal modes of A_g and E_g types.

Table 1 Depicted Raman modes, from the corresponding polarized spectra, with the experimentally determined symmetry assignments. The peak positions (Ω) and damping constants (Full Width at Half Maxima) are in cm^{-1}, as indicated

	Ω (cm^{-1})	FWHM (cm^{-1})		Ω (cm^{-1})	FWHM (cm^{-1})
$A_g(1)$	60.3	0.8	$E_g(1)$	70.5	5.5
$A_g(2)$	85.4	2.5	$E_g(2)$	112.0	1.8
$A_g(3)$	106.5	1.8	$E_g(3)$	120.9	1.9
$A_g(4)$	115.6	1.9	$E_g(4)$	138.5	3.8
$A_g(5)$	150.6	3.4	$E_g(5)$	155.5	6.0
$A_g(6)$	280.9	6.0	$E_g(6)$	201.8	7.4
$A_g(7)$	376.4	7.0	$E_g(7)$	314.5	11.2
$A_g(8)$	391.2	4.7	$E_g(8)$	383.8	3.0
$A_g(9)$	504.0	12.0	$E_g(9)$	401.5	5.6
$A_g(10)$	583.1	15.0	$E_g(10)$	408.0	7.0
$A_g(11)$	733.9	23.5	$E_g(11)$	542.5	16.0
			$E_g(12)$	596.6	18.0
			$E_g(13)$	673.5	8.5
			$E_g(14)$	744.0	20.0

second harmonic generation (SHG) measurements. In the previous section it was shown that despite the polycrystalline nature of our ceramic sample, polarized light allowed to resolve all Raman modes into their appropriate symmetry. Unfortunately, this method cannot be applied for the infrared (polar) modes, once both, used wavelengths and observation regions are far larger than the ceramic grains. Therefore, an attempt to depict the infrared modes was carried out by the analysis of the unpolarized reflectivity spectra of the ceramics (the symmetry assignment of infrared modes is not possible for a non-cubic ceramic).

Fig. 8 shows experimental infrared reflectivity spectra of BCTO at 300 K and 20 K (black lines, vertically shifted for better visualization), beside the adjusted curves from a non-

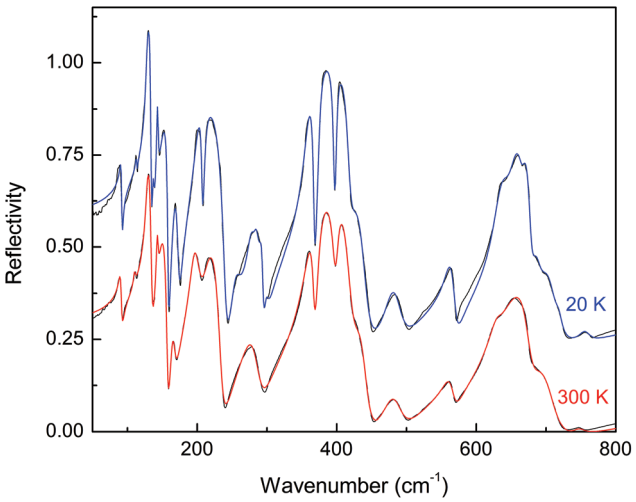

Fig. 8 Experimental (black lines) and fitting curves (blue line, 20 K, and red line, 300 K) of the infrared reflectivity spectra obtained from hexagonal BCTO ceramics.

linear least-square program. Indeed, at low incidence angles, the infrared reflectivity spectrum of a dielectric material is given by the Fresnel law

$$R = \left|\frac{\sqrt{\varepsilon(\omega)} - 1}{\sqrt{\varepsilon(\omega)} + 1}\right|^2 \quad (1)$$

where the complex dielectric dispersion function $\varepsilon(\omega)$, at a wavenumber ω, is given by the contribution of N polar phonons, given, for instance, by its factorized form.[36]

$$\varepsilon(\omega) = \varepsilon_\infty \prod_{j=1}^{N} \frac{\Omega_{j,LO}{}^2 - \omega^2 + i\omega\gamma_{j,LO}}{\Omega_{j,TO}{}^2 - \omega^2 + i\omega\gamma_{j,TO}} \quad (2)$$

In the above expression, ε_∞ is the electronic polarization contribution, Ω is the frequency and γ the damping of the transverse (TO) or longitudinal (LO) phonon branches. Note that, by knowing these four parameters for all N modes (and ε_∞), the infrared dielectric behaviour becomes completely determined (in the case of a ceramic, the averaged "mean field" dielectric constant is determined). Using the Clausius–Mossoti equation, the permittivity value was estimated as 15.7, which is in good agreement with the value of 12.2 extrapolated from the FTIR data.

The fitting procedures used allowed to obtain the polar phonon characteristics of the infrared spectra of BCTO (frequencies and damping constants), listed in Table 2. For the spectrum obtained at 300 K, 19 modes of the 27 predicted ones could be discerned. Therefore, low temperature spectra were necessary to try to resolve all the polar modes. Hence, measurements were performed down to 5 K, and it was observed that the crystal structure is stable in all the temperature range measured, as already observed by other authors.[15,24] However, below 20 K, some pre-transitional effects linked to the AFM phase transition appear, so fitting was preferably

Table 2 Dispersion parameters obtained from the four-parameters semi-quantum model adjust of the infrared reflectivity spectra of BCTO ceramics, at 20 K and 300 K. The wavenumbers (Ω) and damping constants (γ) are in cm^{-1}

20 K		300 K	
Ω_{TO} (γ_{TO})	Ω_{LO} (γ_{LO})	Ω_{TO} (γ_{TO})	Ω_{LO} (γ_{LO})
91.0 (3.2)	92.2 (2.1)	90.3 (4.4)	91.7 (4.0)
113.0 (1.1)	113.1(1.1)	110.4(3.3)	110.5(3.9)
127.5 (4.0)	134.1(2.8)	128.0(5.7)	134.8(5.4)
136.8 (2.7)	137.5(3.3)	—	—
142.6 (2.2)	143.6 (3.3)	142.5 (3.0)	143.3 (3.9)
148.6 (17.3)	158.6 (2.5)	147.3 (14.4)	157.6 (4.7)
167.5 (8.8)	173.6 (6.4)	164.8 (7.6)	167.8 (9.6)
200.3 (14.1)	207.4 (3.7)	194.6 (13.1)	202.4 (18.1)
210.3 (7.8)	240.7 (9.0)	213.9 (24.3)	235.2 (13.0)
255.2 (14.2)	259.0 (19.5)	—	—
278.0 (11.8)	280.7 (10.2)	277.2 (30.1)	290.0 (23.1)
283.6 (9.7)	287.9 (11.4)	—	—
291.8 (7.2)	294.6 (4.5)	—	—
299.0 (7.9)	300.5 (9.6)	—	—
357.6 (12.9)	368.1 (4.2)	360.2 (20.7)	367.8 (6.8)
375.2 (7.0)	396.7 (4.7)	373.5 (12.6)	397.6 (10.5)
398.9 (5.0)	418.5 (13.3)	400.1 (10.2)	420.7 (20.8)
421.5 (19.4)	443.0 (19.4)	427.4 (26.5)	443.5 (19.1)
478.4 (24.4)	491.9 (27.2)	479.3 (33.1)	491.8 (31.1)
562.4 (16.3)	570.5 (11.6)	563.5 (19.0)	567.7 (15.4)
632.2 (20.6)	645.0 (28.2)	629.3 (23.4)	631.7 (22.2)
651.0 (24.9)	665.3 (12.3)	634.4 (53.1)	676.2 (21.0)
666.4 (12.2)	678.0 (10.1)	—	—
681.0 (14.4)	690.0 (20.9)	681.4 (33.6)	710.0 (29.6)
696.0 (24.9)	711.5 (24.6)	—	—
717.8 (12.9)	719.8 (11.8)	—	—
754.9 (19.3)	759.4 (20.7)	745.6 (21.6)	750.0 (23.9)
ε_0 = 15.1; ε_∞ = 3.52		ε_0 = 12.2; ε_∞ = 3.27	

carried out for the 20 K FTIR spectrum to resolve the polar phonon modes. The results are also presented in Table 2. All the 27 polar modes predicted by group theory for hexagonal BCTO could be discerned, and their characteristics listed in that Table 2. It is worth mentioning that low temperature spectra usually allow resolving the modes once they become narrower and stronger, because of the reduction of phonon damping, when lowering the temperature. Therefore, Tables 1 and 2 altogether present the complete set of first-order phonon modes of hexagonal BCTO material.

3.6 Infrared spectra of Ba_2CoTeO_6 around the low-temperature AFM PT

As mentioned in the previous sub-section, low-temperature infrared reflectivity spectra of BCTO showed some additional features around the AFM phase transition. This result is shown in Fig. 9. In Fig. 9(a) shows the infrared reflectivity spectra of BCTO to change very little below 50 K, owing to the high structural stability of the hexagonal room-temperature phase. However, a close look in some specific spectral regions, Fig. 9(b), reveals the appearing of some abnormal features, looking like small dips in the reflectivity spectra below 20 K – indicated by asterisks in the Fig. 9(b).

In order to obtain positions of the spectral anomalies associated to the AFM transitions, Kramers–Kronig calculations were performed on all reflectivity spectra of BCTO (the entire spectral range was used). The results are presented in Fig. 10 and 11, in the form of the imaginary part of the dielectric constant – whose peak positions indicate the frequencies of TO branches (or, in other words, the frequencies of maximum absorption for each vibrational polar mode). Below 20 K, some modes appear to be split into more than one band: the infrared mode at 165.7 cm^{-1} seems to quadruplicate, giving rise to additional features at 161.5, 164.4 and 174.3 cm^{-1}; the mode around 211 cm^{-1} duplicates, giving rise to an additional feature at 217.0 cm^{-1}, as shown in Fig. 10. Similarly, the mode around 562.4 cm^{-1} duplicates originating a new mode at 559.5 cm^{-1}; finally, in the highest frequency region above 610 cm^{-1}, composed by many modes, definitely one new feature appears around 621 cm^{-1}, as marked in Fig. 11.

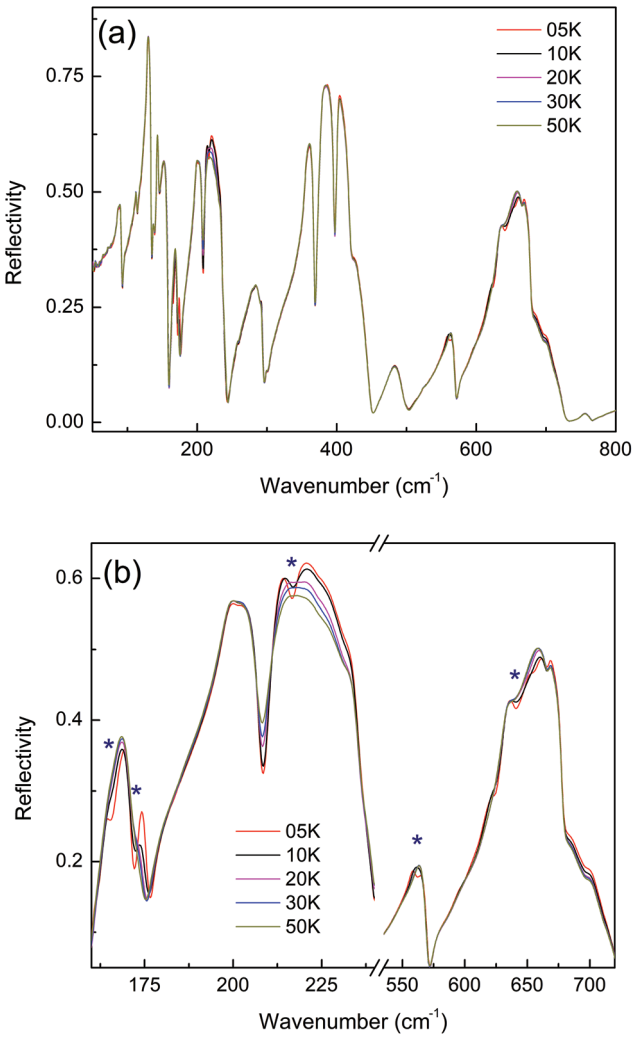

Fig. 9 (a) Infrared reflectivity spectra of BCTO below 50 K. (b) Detail of the low-temperature FTIR reflectivity spectra of BCTO on special spectral regions showing the appearing (asterisks) of small features below the Néel transition (T_N = 12.5 K).

In total, six small absorption-like features are observed in the spectra of Fig. 10 and 11, below T_N. The origin of these

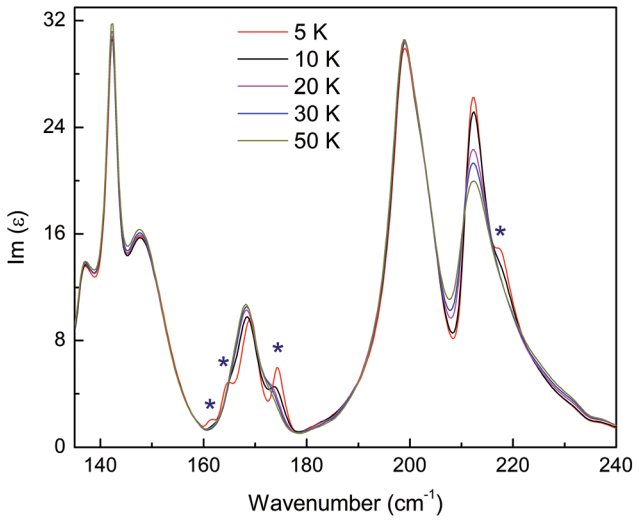

Fig. 10 Imaginary part of the complex dielectric "constant" of BCTO at low temperatures in the 135 to 249 cm^{-1} frequency range. In this frequency region, clear spectral anomalies marked by asterisks appear around the AFM phase transition.

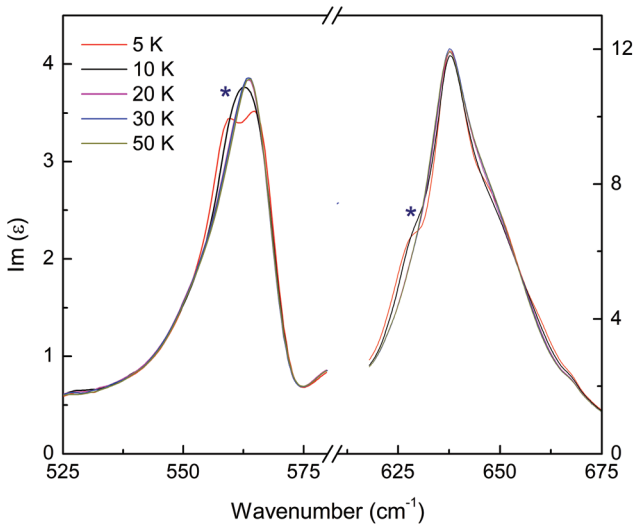

Fig. 11 Imaginary part of the complex dielectric "constant" of BCTO at low temperatures in the 525 to 675 cm^{-1} frequency range. In this frequency region, weaker spectral anomalies marked by asterisks appear around the AFM phase transition.

additional features is not linked to structural changes (the structure is very stable and, as a whole, spectra of Fig. 9–11 show only faint spectral changes), but is in fact linked to small changes in Co–O bond distances and Co–O–Te angle below the AFM phase transition. Indeed, neutron diffraction studies showed that, between 300 K and 5 K Co(1)–O(2) distance decreases by 0.18%, while Co(2)–O(1) and Co(2)–O(3) bonds change by −10.7% and +4.5%, respectively.[15] Besides, Co(1)–O(1)–Te(2) and Co(2)–O(3)–Te(1) angles, which are relevant for the super-exchange mechanisms responsible for the two AFM phase transitions,[24] vary respectively of 0.39% and 1.30%.[15] Therefore, the strong alignment (almost linear) of B and B′ ions along the cubic diagonal of the perovskite BCTO at 5 K is more important for Co(2) ions, *i.e.*, at this temperature the $Co(2)O_6$ sublattice is already into an AFM phase.

Therefore, it is proposed that changes to bond distances and angles involving Co(2) ions are responsible for small distortions of the $Co(2)O_6$ octahedra, lowering locally their C_{3v} symmetry (see Table S4 in ESI†), and splitting the associated vibrational modes (note that there is no long range structural change, only local symmetry lowering).

In terms of electrical conductivity, BCTO ceramics are electrically heterogenous as revealed by the presence of two arcs in the Z^* plot given in Fig. S4 of the ESI.† Based on the brickwork model for electroceramics the low frequency arc may be attributed to a grain boundary component, whereas the higher frequency arc (with an associated capacitance of a few pF) can be ascribed to a bulk response. At 298 K, the total resistance, RT, of the BCTO ceramics is 82 kΩ cm^{-1}, as shown in Fig. S4 in the ESI.† The bulk resistivity can be calculated from the extrapolated intercept of the high frequency semi-arc with the real axis, Z', in Z^* plots. This approach was employed to construct the Arrhenius plot in Fig. 12, which shows the variation in bulk conductivity ($\sigma_b = 1/R_b$) for 6L-BCTO ceramics. Literature bulk conductivities for 6H-$BaTiO_3$ and 6H-$Ba_2MnTiO_{5.68}$ ceramics are also included for comparison.[7] Data for those two compounds were included because both are 6-layered hexagonal perovskites homologous to BCTO, *i.e.* their crystal structure consists of two face-sharing octahedra connected by one corner-sharing octahedron, arising from the *abcacb* stacking sequence of the AO_3 closed-packed layers. Nevertheless, their electrical behaviour is dramatically different. Indeed, undoped 6H-$BaTiO_3$ is electrically insulating at room temperature and has an activation energy for conduction, E_a of ∼1 eV. In contrast, 6H-$Ba_2MnTiO_{5.68}$ is a "leaky insulator/semiconductor" at room temperature with E_a ∼0.36 eV.

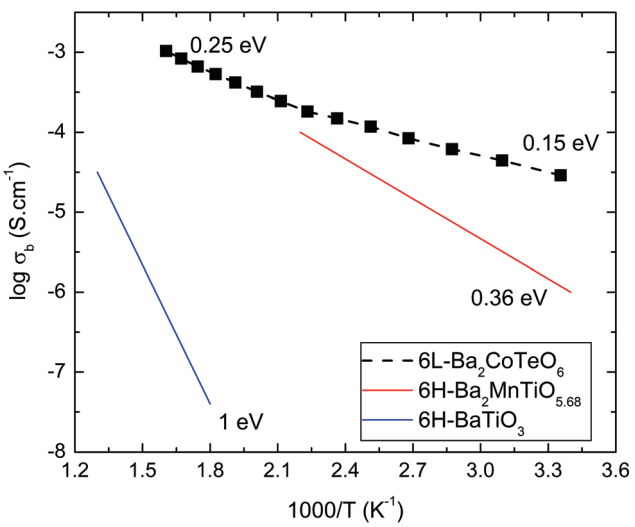

Fig. 12 Arrhenius plot for the electrical conductivity of BCTO. Data for 6H-$Ba_2MnTiO_{5.68}$ from ref. 7.

Miranda *et al.*[7] postulated that the higher conductivity and lower E_a exhibited by 6H-$Ba_2MnTiO_{5.68}$ in comparison with 6H-$BaTiO_3$ is to be associated with the oxygen deficiency and mixed valency of the Mn ions. The latter promoting a change in electrical conduction from a band type mechanism in undoped 6H-$BaTiO_3$ to electron hopping between Mn cations by a phonon-assisted process in 6H-$Ba_2MnTiO_{5.68}$. BCTO ceramics exhibit an electrical behaviour closer to that of 6H-$Ba_2MnTiO_{5.68}$, but even with a lower E_a in the low temperature range, as shown in Fig. 12. BCTO ceramics also exhibit a non-Arrhenius-type response as indicated by the slight deviation from linearity over the temperature range of the measurement. Hence, the electrical behaviour of BCTO ceramics may be linked either to mixed oxidation of Co and/or the presence of different conduction mechanisms, each one contributing in a temperature region within the range investigated. Miranda *et al.*[7] encounter a similar response in ceramics based on the hexagonal perovskite 12R-$BaMn_{2/3}Ti_{1/3}O_3$, which contrasted with an Arrhenius-type response observed by Keith *et al.*[37] in 12R-$BaMn_{1/2}Ti_{1/2}O_3$ ceramics. At 298 K, the bulk permittivity was calculated as ~65, which is within the range of values measured for other hexagonal perovskites.

4. Conclusions

Ba_2CoTeO_6 ceramics exhibit a hexagonal perovskite structure, whose internal symmetry can be well described by $P\bar{3}m1$ space group as corroborated by XRD, FTIR and Raman data. Those results are in broad agreement with previous structural studies employing neutron diffraction.[15] On cooling from room-temperature, Ba_2CoTeO_6 ceramics exhibit two antiferromagnetic transitions at 3 K and 12.5 K, respectively, again in broad agreement with a recent single-crystal study.[24] This corroborates the good quality of the ceramics prepared in this study. Temperature dependent FTIR analysis show that the antiferromagnetic phase transitions are driven by changes to bond distances and angles involving Co(2) ions, which are responsible for small distortions of the $Co(2)O_6$ octahedra, lowering locally their C_{3v} symmetry. In terms of electrical properties, BCTO ceramics can be regarded as leaky insulators, with a bulk resistance lower than 35 kΩ cm^{-1} and an activation energy for electrical conduction of 0.15–0.25 eV. In addition, the present study shows the purity of Ba_2CoTeO_6 ceramics to be dramatically affected by the maximum firing temperature. Indeed, single-phase Ba_2CoTeO_6 ceramics can be successfully synthesised at 1350 °C. However above this temperature, surface decomposition due to volatilisation of Co leads to the formation of Ba_3TeO_6, as a secondary phase.

Conflicts of interest

There are no conflicts to declare.

Acknowledgements

Anees Aziz acknowledges financial support from Majlis Amanah Rakyat-Malaysia for the PhD studies. The magnetic measurements at ESPCI have been supported through Grants from Region Ile-de-France. AD and RLM are grateful for the funding received from the Brazilian agencies CNPq, FINEP and FAPEMIG. RLM also acknowledges ESPCI for a "Chaire Joliot" appointment.

References

1 J. S. Dean, P. Y. Foeller, I. M. Reaney and D. C. Sinclair, *J. Mater. Chem. A*, 2016, **4**, 6896–6901.
2 M. D. Glinchuk, I. P. Bykov, S. M. Kornienko, V. V. Laguta, A. M. Slipenyuk, A. G. Bilous, O. I. V'Yunov and O. Z. Yanchevskii, *J. Mater. Chem.*, 2000, **10**, 941–947.
3 F. Shi and H. L. Dong, *Dalton Trans.*, 2011, **40**, 6659–6667.
4 Y. P. Guo, Y. Liu, R. L. Withers, F. Brink and H. Chen, *Chem. Mater.*, 2011, **23**, 219–228.
5 B. Y. Zhang, J. G. Wu, X. J. Cheng, X. P. Wang, D. Q. Xiao, J. G. Zhu, X. J. Wang and X. J. Lou, *ACS Appl. Mater. Interfaces*, 2013, **5**, 7718–7725.
6 L. Miranda, K. Boulahya, A. Varela, J. M. Gonzalez-Calbet, M. Parras, M. Hernando, M. T. Fernandez-Diaz, A. Feteira and D. C. Sinclair, *Chem. Mater.*, 2007, **19**, 3425–3432.
7 L. Miranda, A. Feteira, D. C. Sinclair, K. Boulahya, M. Hernando, J. Ramirez, A. Varela, J. M. Gonzalez-Calbet and M. Parras, *Chem. Mater.*, 2009, **21**, 1731–1742.
8 L. Miranda, A. Feteira, D. C. Sinclair, M. G. Hernandez, K. Boulahya, M. Hernando, A. Varela, J. M. Gonzalez-Calbet and M. Parras, *Chem. Mater.*, 2008, **20**, 2818–2828.
9 A. Feteira, G. Keith, M. Rampling, C. Kirk, I. Reaney, K. Sarma, N. Alford and D. Sinclair, *Cryst. Eng.*, 2002, **5**, 439–448.
10 G. Bayer, *J. Am. Ceram Soc.*, 1963, **46**, 604.
11 G. Bayer, *US Pat*, 3309168, 1967.
12 P. Köhl, U. Muller and D. Reinen, *Z. Anorg. Allg. Chem.*, 1972, **392**, 124–136.
13 M. Liegeoisduyckaerts, *Spectrochim. Acta, Part A*, 1975, **31**, 1585–1588.
14 M. Liegeoisduyckaerts, *Spectrochim. Acta, Part A*, 1985, **41**, 523–529.
15 S. A. Ivanov, P. Nordblad, R. Mathieu, R. Tellgren and C. Ritter, *Dalton Trans.*, 2010, **39**, 5490–5499.
16 F. Sher and J. P. Attfield, *Solid State Sci.*, 2006, **8**, 277–279.
17 U. Treiber and S. Kemmlersack, *Z. Anorg. Allg. Chem.*, 1980, **470**, 95–102.
18 E. D. Politova and V. Yn, *Dokl. Akad. Nauk SSSR*, 1973, **209**, 838–841.
19 E. D. Politova and Y. N. Venevtsev, *Mater. Res. Bull.*, 1975, **10**, 319–325.
20 Y. N. Venevtsev, E. D. Politova and G. S. Zhdanov, *Ferroelectrics*, 1974, **8**, 489–490.
21 N. A. Hill, *J. Phys. Chem. B*, 2000, **104**, 6694–6709.

22 T. Zhao, A. Scholl, F. Zavaliche, K. Lee, M. Barry, A. Doran, M. Cruz, Y. Chu, C. Ederer, N. Spaldin, R. Das, D. Kim, S. Baek, C. Eom and R. Ramesh, *Nat. Mater.*, 2006, **5**, 823–829.
23 R. Mathieu, S. A. Ivanov, R. Tellgren and P. Nordblad, *Phys. Rev. B: Condens. Matter Mater. Phys.*, 2011, **83**, 6.
24 P. Chanlert, N. Kurita, H. Tanaka, D. Goto, A. Matsuo and K. Kindo, *Phys. Rev. B: Condens. Matter Mater. Phys.*, 2016, **93**, 094420.
25 H. Tanaka, N. Kurita, M. Koike, M. Jaime and D. F. Weickert, *P13631-E002PF Pulsed field magnetostriction of Ba_2CoTeO_6*, 2017.
26 Y. Shirata, H. Tanaka, A. Matsuo and K. Kindo, *Phys. Rev. Lett.*, 2012, **108**, 057205.
27 W. Hayes and R. Loundon, *Scattering of Light by Crystals*, Wiley, New York, 1978.
28 D. K. Kwon, M. T. Lanagan and T. R. Shrout, *Mater. Lett.*, 2007, **61**, 1827–1831.
29 R. L. Moreira, R. Lobo, S. Ramos, M. T. Sebastian, F. M. Matinaga, A. Righi and A. Dias, *Phys. Rev. Mater.*, 2018, **2**, 054406.
30 A. Dias, L. A. Khalam, M. T. Sebastian, C. William, C. W. A. Paschoal and R. L. Moreira, *Chem. Mater.*, 2006, **18**, 214–220.
31 A. Dias, F. M. Matinaga and R. L. Moreira, *Chem. Mater.*, 2007, **19**, 2335–2341.
32 A. Dias, L. A. Khalam, M. T. Sebastian, M. M. Lage, F. M. Matinaga and R. L. Moreira, *Chem. Mater.*, 2008, **20**, 5253–5259.
33 A. Dias, G. Subodh, M. T. Sebastian, M. M. Lage and R. L. Moreira, *Chem. Mater.*, 2008, **20**, 4347–4355.
34 A. Dias, M. M. Lage, L. A. Khalam, M. T. Sebastian and R. L. Moreira, *Chem. Mater.*, 2011, **23**, 14–20.
35 D. Rousseau, R. Bauman and S. Porto, *J. Raman Spectrosc.*, 1981, **10**, 253–290.
36 F. Gervais and P. Echegut, in *Incommensurate phases in dielectrics*, ed. R. Blinc and A. P. Levanyuk, North Holland, Amesterdam, 1986, p. 337.
37 G. M. Keith, C. A. Kirk, K. Sarma, N. M. Alford, E. J. Cussen, M. J. Rosseinsky and D. C. Sinclair, *Chem. Mater.*, 2004, **16**, 2007–2015.